

Holocene ice-stream shutdown and drainage basin reconfiguration in northeast Greenland

Received: 6 November 2021

Accepted: 20 October 2022

Published online: 05 December 2022

 Check for updates

Steven Franke¹✉, Paul D. Bons^{2,3}, Julien Westhoff⁴, Ilka Weikusat^{1,2}, Tobias Binder¹, Kyra Streng², Daniel Steinhage¹, Veit Helm¹, Olaf Eisen^{1,5}, John D. Paden⁶, Graeme Eagles¹ & Daniela Jansen¹

Reliable knowledge of ice discharge dynamics for the Greenland ice sheet via its ice streams is essential if we are to understand its stability under future climate scenarios. Currently active ice streams in Greenland have been well mapped using remote-sensing data while past ice-stream paths in what are now deglaciated regions can be reconstructed from the landforms they left behind. However, little is known about possible former and now defunct ice streams in areas still covered by ice. Here we use radio-echo sounding data to decipher the regional ice-flow history of the northeastern Greenland ice sheet on the basis of its internal stratigraphy. By creating a three-dimensional reconstruction of time-equivalent horizons, we map folds deep below the surface that we then attribute to the deformation caused by now-extinct ice streams. We propose that locally this ancient ice-flow regime was much more focused and reached much farther inland than today's and was deactivated when the main drainage system was reconfigured and relocated southwards. The insight that major ice streams in Greenland might start, shift or abruptly disappear will affect future approaches to understanding and modelling the response of Earth's ice sheets to global warming.

Satellite observations of current surface flow of the ice sheets in Greenland (GrIS) and Antarctica reach back to the 1970s^{1–3}. Reconstructions of earlier ice-stream activity are based mostly on their geomorphological imprints in formerly glaciated regions but are limited to the period since the Last Glacial Maximum^{4,5}. These reconstructions show that ice streams were activated and deactivated in different locations and at different times during the post-Last Glacial Maximum deglaciation (22–7 thousand years (ka) ago). Patterns of former ice flow in regions that are still covered by ice sheets may be revealed by folds in internal reflection horizons (IRHs) that are

visible in high-quality radio-echo sounding (RES) data^{6–9}. Most IRHs are considered to be buried former snow layers deposited on the surface of the ice sheets¹⁰. Englaciation deformation can disturb the conformity and continuity of IRHs and lead to a non-monotonically increasing age distribution with depth, which is a challenge for ice-core analysis¹¹.

Folds in the GrIS and Antarctic ice sheet range from centimetre-scale folding observed in ice cores^{12–14} to folds that affect nearly the entire ice column^{15,16}. RES data have revealed the presence of overturned and sheath folds and plume-like structures overlying broad

¹Alfred Wegener Institute, Helmholtz Centre for Polar and Marine Research, Bremerhaven, Germany. ²Department of Geosciences, Tübingen University, Tübingen, Germany. ³China University of Geosciences, Beijing, China. ⁴Physics of Ice, Climate and Earth, Niels Bohr Institute, University of Copenhagen, Copenhagen, Denmark. ⁵Department of Geosciences, University of Bremen, Bremen, Germany. ⁶Center for Remote Sensing and Integrated Systems (CReSIS), University of Kansas, Lawrence, KS, USA. ✉e-mail: steven.franke@awi.de

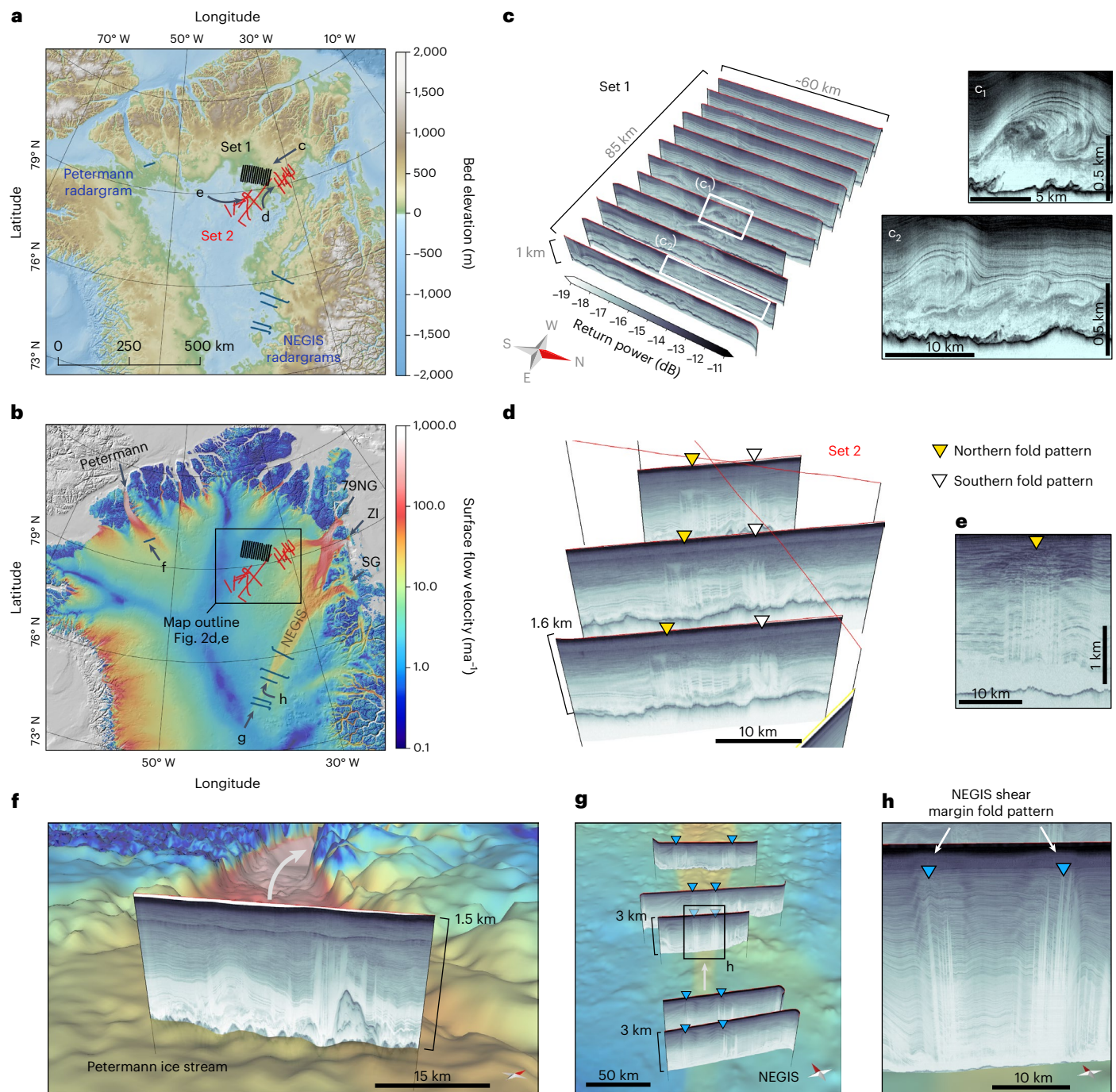


Fig. 1 Overview of the study site and key RES observations. **a, b**, Northern Greenland's bed topography (**a**)⁴⁴ and ice surface velocity (**b**)²⁷ with the locations of two sets of RES profile lines (Set 1 in black and Set 2 in red). The black rectangle indicates the map outline of Fig. 2d,e. The major outlets in northeast Greenland are indicated with black arrows (79NG, 79° North Glacier (Nioghalvfjærdsbrae); ZI, Zachariae Isstrom; SG, Storstrømmen Glacier). **c**, Selected RES profiles of Set 1.

d, A subset of three radargrams of Set 2 with a repeating radar signature. **e**, A radargram of Set 2 with a characteristic radar signature in the upstream region **f**, A radargram from the onset of the Petermann ice stream. **g**, Radargrams at the onset of NEGIS (see **b**). **h**, A radargram showing the NEGIS shear margin fold pattern (see **g**). The white arrows in **f** and **g** indicate today's general ice-flow direction, looking downstream.

areas of disrupted basal stratigraphy^{8,9,17,18}. A range of processes has been proposed to explain the diversity of folding, including basal freeze-on^{9,18–20}, contrasts in ice rheology¹², changes in basal resistance^{21,22} and convergent flow¹⁷.

In this Article, we combine recently acquired and older RES data over the northeast GrIS to reconstruct former flow patterns. Our findings reveal the Holocene activity of two now-extinct ice streams in an area close to the present-day ice divide.

Radiostratigraphy

We consider RES profiles in northeast Greenland upstream of the northern catchment of the Nioghalvfjærdsbrae (79° N Glacier (79NG); Fig. 1a–d) acquired by NASA's Operation IceBridge (OIB) and by the Alfred Wegener Institute, Helmholtz Centre for Polar and Marine Research (AWI). The RES profiles in Fig. 1c (Set 1, black profiles in Fig. 1a,b) were acquired with AWI's multi-channel ultra-wideband (UWB) radar system in 2018. Ice surface velocity is almost zero in the west of Set

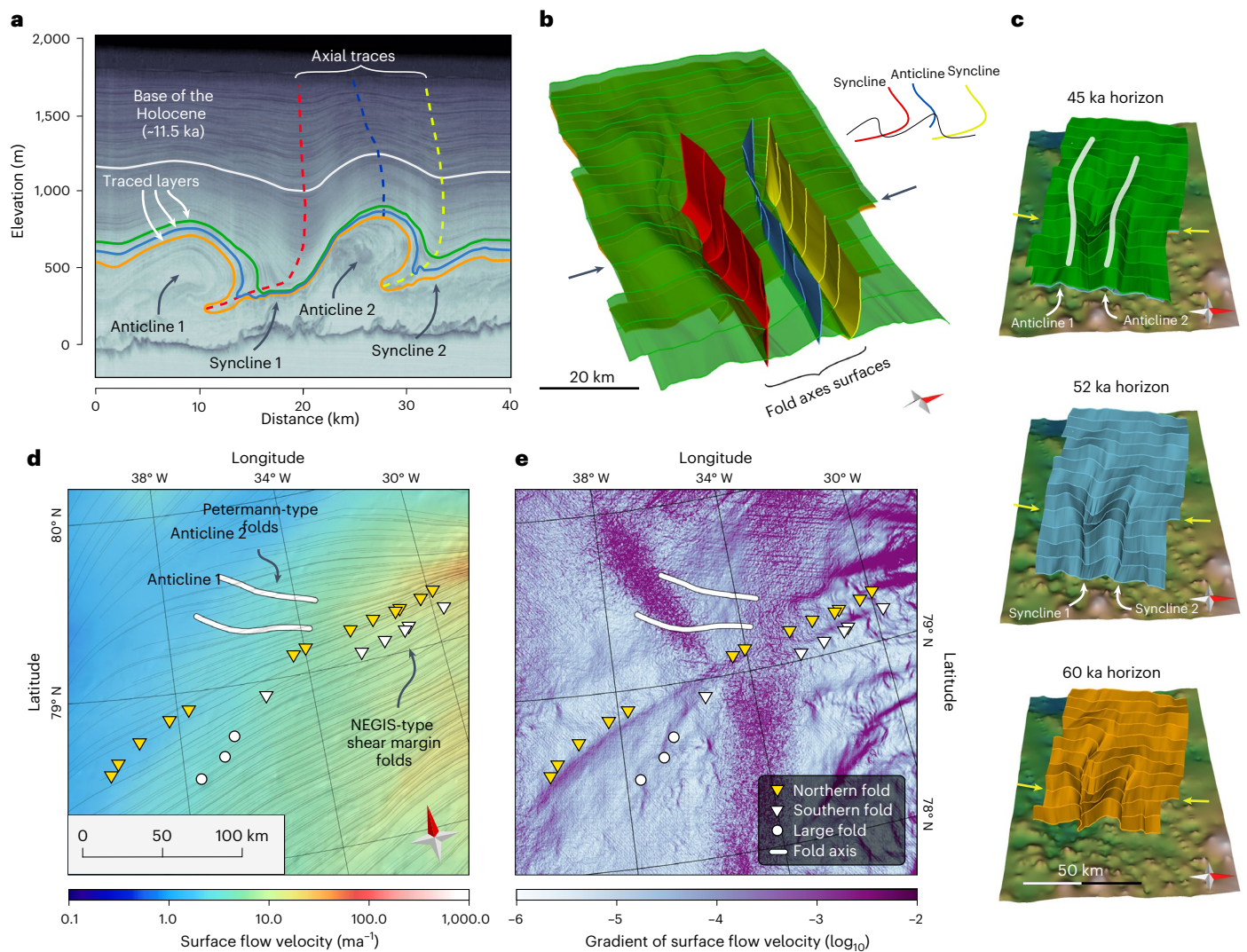


Fig. 2 | Folded radiostratigraphy in northeast Greenland. **a**, Radargram of Set 1 with three traced internal reflections (green, pale blue and orange; 45 ka, 52 ka and 60 ka, respectively) and axial planes of two synclines (red and yellow) and one anticline (dark blue). The base of the Holocene ice column (~11.5 ka) is highlighted with a white line. **b**, The reconstructed 3D internal horizons and axial surfaces. **c**, The individual horizons. The location of the radargram in **a** is indicated with

yellow arrows. **d,e**, Overview of the locations of these Petermann-type folds (two cylindrical anticlines of Set 1) and the NEGIS-type shear margin folds (tight fold sequences) superimposed on the ice surface velocity²⁷ (**d**) and superimposed on the gradient of that velocity on a logarithmic scale (\log_{10}) (**e**). The background map in **c** shows the bed topography (Supplementary Fig. 17b).

1 close to the ice divide and increases eastwards to as much as 15 m a^{-1} (Extended Data Fig. 1). The survey was designed to closely investigate a set of folds already detected in earlier surveys²³. Twelve RES profiles were flown, at 7.5 km spacing, and oriented perpendicular to the 100° true North trend of the fold axes (Extended Data Figs. 1 and 2 and Supplementary Figs. 1–12). We mapped cylindrical folds that reach their highest amplitudes at the centres of the RES profiles (Extended Data Fig. 3). The fold shapes and orientations do not mimic the underlying bed topography (Supplementary Figs. 13 and 14 and Extended Data Fig. 4). Similar folds have been observed at multiple locations in the GRIS^{8,9,18,21}, including upright cylindrical folds in the active convergent flow region of Petermann ice stream in northwest Greenland¹⁷ (Fig. 1f).

The RES profiles of Set 2 (Fig. 1a,b,d and Supplementary Fig. 15) are composed of OIB and AWI profiles acquired with different RES systems. They extend from the central divide eastwards into the northern catchment of the 79NG. The radargrams reveal a recurring signature of vertical stripes of low reflectivity in the lower two-thirds of the ice column (Fig. 1d,e (yellow and white markers), Extended Data Fig. 5 and Supplementary Figs. 16–21), which results from the loss of

reflected energy from steeply dipping internal layers whose steepness increases with depth²⁴. The pattern of these features and their appearance in multiple radargrams (Fig. 1d and Extended Data Fig. 5) bears a strong resemblance to similar features within the shear margins of the Northeast Greenland Ice Stream (NEGIS; Fig. 1g,h and Supplementary Figs. 24–29; fig. 7a in ref. ²⁵ and fig. 3 in ref. ¹⁵).

A palaeo ice stream analogous to the Petermann ice stream

We traced three IRHs with estimated ages of 45, 52 and 60 ka (ref. ²⁶) in the lower part of the ice column that are continuously visible in all radargrams (Fig. 2a–c). We reconstructed the shapes of the three stratigraphic horizons by interpolating surfaces between the IRHs in our RES profiles (Methods). This reveals two parallel cylindrical anticline–syncline pairs (Fig. 2b,c) whose geometry was validated using an OIB RES section oriented obliquely to the fold axes (Supplementary Fig. 13). The internal layers are folded far up into the base of the Holocene ice column (Fig. 2a). The steepest upper parts of the axial planes strike east–west with a shallowing of the dip at the base that suggests top-to-the-north

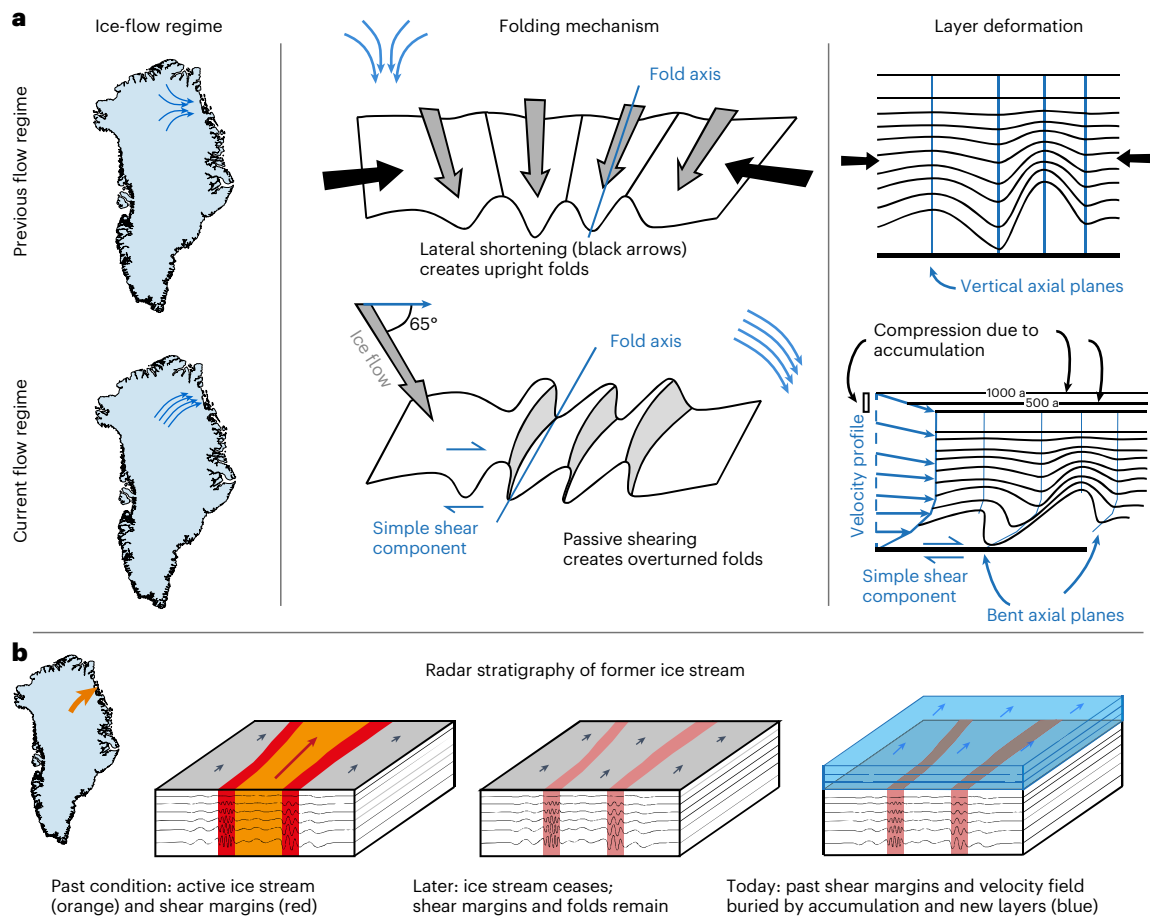


Fig. 3 | Conceptual model for the ice-dynamic reconstruction from fold patterns. **a**, The formation of overturned cylindrical folds of Set 1. The upper row illustrates the formation of upright folds due to a convergent palaeo flow regime. The row below indicates a change from the palaeo flow regime to the present flow regime, which passively shears the upright folds. The schematic ice-flow regime is indicated in the left column, the effects of the flow mechanisms on the folds are illustrated with a 3D horizon in the middle column and the schematic

layer deformation in a 2D radargram is in the right column. **b**, The reconstructed sequence of flow regimes producing the observed RES stratigraphy patterns in Set 2. An active NEGIS-type ice stream with localized ice flow (orange) created the tight folds at its shear margins (red). Later, ice flow ceased and subsequent accumulation buried the folded layers beneath younger flat layers (blue), compressing them. Outline of Greenland from QGreenland, NSIDC⁴⁵.

bedrock-parallel shearing (Fig. 2b). The reconstructed folds show a strong resemblance to the folds at the onset region of the active Petermann ice stream, which are suggested to be products of convergent flow and lateral shortening¹⁷. In contrast to the Petermann folds, they are systematically overturned towards the north. They have smaller amplitudes than their Petermann counterparts, and their fold axes lie oblique (by -25°), rather than parallel to present-day flow direction¹⁷ (Fig. 2d and Extended Data Fig. 4b).

Folds similar to the shear margins folds of NEGIS

We find characteristic upright, short-wavelength (~ 100 – 500 m) folds with amplitudes up to ~ 100 m extending almost from the ice divide to the northern catchment of the 79NG in the RES stratigraphy of Set 2 (Figs. 1b,d and 2d,e, Extended Data Fig. 5 and Supplementary Figs. 15–21 for details). Especially in the downstream portion of Set 2, these bear a remarkable resemblance to folds in the shear margins of the active NEGIS (Fig. 1d,e,g,h, Extended Data Fig. 6 and Supplementary Figs. 24–29). Set 2 reveals further similarities between the folds in our survey area and the NEGIS-type folds, including downwarping internal layers at the outer margins of the fold sequences, kink folds in the region between them (Extended Data Fig. 6) and characteristic reflections in RES profiles oriented obliquely to the fold axes (Supplementary Fig. 27). The folds at the active shear margins of NEGIS extend almost up

to the ice surface, and the folds in Set 2 clearly disrupt the stratigraphy of the base of the Holocene (~ 11.5 ka; Extended Data Fig. 6). Furthermore, the folds in Set 2 coincide with a southwest–northeast-trending zone of slightly elevated surface velocity gradient that extends far upstream (Fig. 2e and Supplementary Fig. 22). A second trail of folds to the southeast is less pronounced, and far upstream, we find only solitary large folds, including one that was previously interpreted as bedrock (Supplementary Fig. 23).

Folding sequences and ice flow

Three different mechanisms for the origin of folds as in Set 1 have been proposed: basal freeze-on¹⁸, variations in basal resistance²¹ and response to convergent ice flow¹⁷. Folds resulting from basal freeze-on or basal-resistance effects are expected to trend perpendicular to the direction of ice flow¹⁷, thus, north–south in our study region. Similarly, present-day ice flow in the region of the folds is not convergent²⁷. The current local flow regime can therefore not explain the occurrence of the observed folds. All three folding mechanisms^{17,18,21} require ice to flow in a given direction for a long period, but the inferred direction of ice flow is different for basal freeze-on and variations in basal resistance than for folding by convergent flow. According to the direction of the fold axes (which is determined by the orientation of the fold hinges) and the direction of overturning, ice flow should have been northwards

if the folds were created by freeze-on or variations in basal resistance (Extended Data Fig. 4a,b). Fold formation by convergent flow would imply a flow direction parallel to the fold axes, which would thus be eastwards. A constant northward flow over a longer period is unlikely considering that outlet glaciers in the north are much smaller than in the east (Extended Data Fig. 4a,b). Furthermore, folding due to freeze-on and variations in basal resistance would require highly complex basal properties (for example, recurrent alternations of melting and freezing to create pairs of anticlines and synclines) for which there is no evidence (Extended Data Fig. 4c,d and Supplementary Section 1.3).

Therefore, on the basis of the three-dimensional (3D) geometry, glaciological setting and orientation of the folds, we consider the following two-stage scenario as the most likely one to explain initial fold formation and subsequent deformation (Fig. 3a). In the first stage, a convergent flow regime similar to the one in the onset zone of today's Petermann ice stream created large upright folds. The axes of folds formed in such settings align with the positions of today's major outlets in northeast Greenland (Figs. 1 and 4). The greater number of folds downstream (Extended Data Fig. 3) indicates an increase in the intensity of folding due to an increase in horizontal shortening. In the second stage, the flow regime had changed to its present configuration. Ice flow is oblique to the previous flow direction but no longer convergent, resulting in wholesale bedrock-parallel shearing of the existing folds (Fig. 3a). Applying the current flow field to restore the shearing and reconstruct a set of upright folds requires a period of at least 1.0–2.5 ka (Supplementary Fig. 31 and Supplementary Table 1). This is a minimum estimate as we do not know the exact geometry of the axial planes before shearing (Supplementary Fig. 31). Ongoing accumulation without further fold growth would have led to compression of the folds, reducing their amplitudes. Along-flow stretching and shearing during this second phase of deformation appears to have affected the downstream portion of the mapped features more strongly due to the higher ice-flow velocities there.

The similarities of the RES signatures in Set 2 to radargrams observed at NEGIS suggest that the observed features are remnants of the shear margins of a now-extinct ice stream (Fig. 3b, Extended Data Figs. 5 and 6 and Supplementary Section 2). As folds act as passive tracers of ice deformation, remnants of past ice-stream activity are still visible even if the shear zone is no longer active. These observations suggest that the folding in Set 2 is the product of a ~20-km-wide palaeo ice stream with distinct shear margins similar to the currently active NEGIS (Fig. 3b).

By reconstructing folds from structural information archived in the RES stratigraphy, we have revealed the extents and characteristics of two palaeo ice streams (one Petermann type and one NEGIS type) in the northern 79NG catchment, both of which originally extended far into the ice-sheet interior (Fig. 4). It is difficult to ascertain exactly when the ice streams were active. Assuming it to be likely that the deformation processes are younger than the deformed radar stratigraphy, both ice streams can be shown to have been active into the Holocene, whose basal reflector (~11.5 ka) is deformed by both sets of folds (Fig. 2a and Extended Data Fig. 6b). The lateral shearing of the Petermann-type folds is on the order of 10–20 km (Fig. 3a). At the current surface velocity of ~3–5 m a⁻¹, the lateral shearing must thus have operated for at least ~2.5 ka since formation of the folds. This is consistent with the youngest ice layers not showing substantial folding. Another possibility could be that the two palaeo ice streams do not represent synchronous separate events but instead evolutionary stages of a larger, evolving ice-stream system.

Ice streams come and go

Numerical modelling studies suggest that ice streams with highly localized shear margins can spontaneously appear by self-reinforcing processes within ice sheets^{28–32}. These studies all require an initial instability to activate the feedback loop that enforces flow localization.

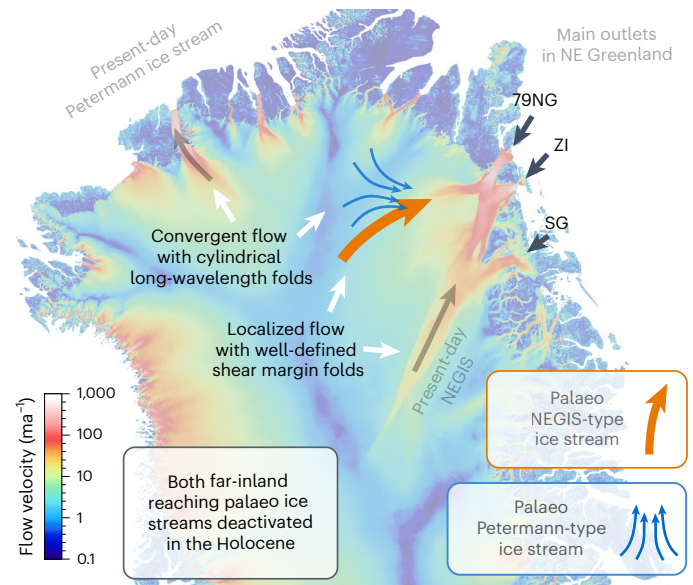


Fig. 4 | Illustration of the palaeo ice-stream locations in northeast Greenland.

The exact positions of the two palaeo ice streams during their active lifetimes depend on the temporal evolution of the ice-flow field since their deactivations (Extended Data Fig. 7). Magnitudes of present ice-flow velocities in Greenland²⁷ are in the colour-coded background, and superimposed are the former convergent flow regime (blue arrows) and the NEGIS-type ice stream (orange arrow).

This instability can be generated by coupling of the temperature field and ice flow using simplifications such as the shallow ice approximation²⁹, but yields more consistent results by implementing longitudinal stresses (membrane stress approximation³⁰). Schoof and Mantelli³¹ show similar patterns emerging due to a feedback of temperature and sliding at the bed. The study by Syag et al.³² presents temporally variable ice-stream systems, which switch between 'catchment' areas feeding the stream, depending on perturbations in the driving stresses. All of these studies use simplified, artificial geometry set-ups for their simulations as they all focus on investigating mechanisms and do not aim to simulate any particular real ice streams. Despite this, their results support the view that spontaneous localization of self-reinforcing flow by any of a number of mechanisms is likely to be a process that leaves observable traces in real ice sheets. These processes require no further evidence to be consistent with our observations of ice-stream products deep in the interior of the GrIS.

Our study provides extensive observational evidence that ice streams are temporally and spatially variable components of the northeast GrIS. The mechanisms and boundary conditions required for flow regimes to reorganize and generate ice streams in new locations are not yet fully understood. The initiation and termination of fast flow could be considered a particular case of surging behaviour³³, whose specific properties vary according to temporally changing combinations of climate, ice-sheet geometry and bed properties, for example, the rearrangement of water routing networks³⁴. However, in situ observations of some of these properties and detailed dating of our palaeo ice streams are still lacking, making it difficult to fully test and quantify this possibility for the northeast GrIS.

Flow regime shifts on similar spatio-temporal scales to our observations have previously been demonstrated around the outlets of the Siple Coast ice streams in Antarctica^{35–37}. One, the active Bindschadler Ice Stream (formerly Ice Stream D), presents a single large fold that has been argued³⁸ to have experienced shearing after originally forming as an upright flow-parallel fold, very similar to the multiple folds documented here. The switching behaviour of the Siple Coast ice streams has been related to the competition for ice discharge

between neighbouring basins during a period of regional ice-sheet thinning³⁷. A similar line of argument is followed by Stokes et al.⁵ in a reconstruction-based study of the Laurentide Ice Sheet. They suggest that streaming was triggered at times of large ice volume and that it ceased abruptly during volume reductions. Hence, ice-stream initiation is particularly likely to occur at the beginning of deglaciations. Geological evidence³⁹ and modelling studies⁴⁰ that indicate substantial changes in the geometry and elevation of the GrIS over the Holocene are consistent with this hypothesis. On the basis of the coarse dating that is possible, we suggest that a Holocene north-to-south reconfiguration of the ice-sheet geometry in northeast Greenland either (1) deactivated both northern palaeo ice streams, where the NEGIS and the palaeo NEGIS-type ice stream were simultaneously active or (2) relocated the main far-inland reaching ice drainage system southwards by deactivating the northern palaeo ice streams and initiating localized ice flow at the onset region of the NEGIS (Fig. 4). The latter possibility suggests that the upstream part of the present-day NEGIS is relatively young.

The evidence for the activity of a former ice stream with well-defined shear zones is also of major importance for ongoing research into comparable present-day ice streams. Today's NEGIS is a prominent feature whose origin and activity have been controversially related to exceptionally high geothermal heat flux (GHF) at its onset^{41,42}. However, the existence of such a high GHF was challenged⁴³. Our discovery of an extinct ice stream that would have had very similar properties, but was located well to the north of today's NEGIS, adds to the range of observations that suggest localized high GHF is not necessarily a prerequisite for NEGIS-type flow. Our observation that the palaeo NEGIS-type and Petermann-type ice-flow systems extended much farther inland than the present flow field at this location (Fig. 4) indicates that effective ice drainage expands or retreats depending on the ice discharge conditions forced by the overall glaciological setting. As a consequence, the divide between the eastern and northwestern catchments may have shifted to the west when the palaeo ice stream was active and possibly back to the east again after its deactivation. This has consequences for our interpretation of deep drilling projects (NEEM, NGRP, GRIP and so on) that are now on divides or domes, but may not always have been so during the Holocene.

Identifying the location, type and, if possible, time of activity of palaeo ice streams in the GrIS is of paramount importance for understanding ice-stream longevity and their past and future activity. Our observations provide a benchmark for the interpretation of other proxies of past ice-dynamic activity, for example, sedimentation rates and characteristics obtained from marine sediment records off the Greenland east coast. The reproducibility of our findings in models is particularly important to increase our confidence about whether, how and how suddenly the GrIS might reconfigure in response to ongoing mass changes and loss. Our work highlights that ice-stream activity is subject to temporal changes also on the larger ice-sheet scale and that the processes governing these changes need to be better understood and implemented in numerical models to accurately predict Greenland's and Antarctica's evolving contributions to sea-level rise in the future.

Online content

Any methods, additional references, Nature Portfolio reporting summaries, source data, extended data, supplementary information, acknowledgements, peer review information; details of author contributions and competing interests; and statements of data and code availability are available at <https://doi.org/10.1038/s41561-022-01082-2>.

References

- Rosenau, R., Scheinert, M. & Dietrich, R. A processing system to monitor Greenland outlet glacier velocity variations at decadal and seasonal time scales utilizing the Landsat imagery. *Remote Sens. Environ.* **169**, 1–19 (2015).
- Rignot, E. et al. Four decades of Antarctic Ice Sheet mass balance from 1979–2017. *Proc. Natl Acad. Sci. USA* **116**, 1095–1103 (2019).
- Mouginot, J. et al. Forty-six years of Greenland Ice Sheet mass balance from 1972 to 2018. *Proc. Natl Acad. Sci. USA* **116**, 9239–9244 (2019).
- Margold, M., Stokes, C. R. & Clark, C. D. Ice streams in the Laurentide Ice Sheet: identification characteristics and comparison to modern ice sheets. *Earth Sci. Rev.* **143**, 117–146 (2015).
- Stokes, C. R., Margold, M., Clark, C. D. & Tarasov, L. Ice stream activity scaled to ice sheet volume during Laurentide Ice Sheet deglaciation. *Nature* **530**, 322–326 (2016).
- Rodriguez-Morales, F. et al. Advanced multifrequency radar instrumentation for polar Research. *IEEE Trans. Geosci. Remote Sens.* **52**, 2824–2842 (2014).
- Gogineni, S. et al. Coherent radar ice thickness measurements over the Greenland ice sheet. *J. Geophys. Res. Atmos.* **106**, 33761–33772 (2001).
- MacGregor, J. A. et al. Radiostratigraphy and age structure of the Greenland Ice Sheet. *J. Geophys. Res. Earth Surf.* **120**, 212–241 (2015).
- Bell, R. E. et al. Deformation warming and softening of Greenland's ice by refreezing meltwater. *Nat. Geosci.* **7**, 497–507 (2014).
- Robin, G. D. Q., Evans, S. & Bailey, J. T. Interpretation of radio echo sounding in polar ice sheets. *Phil. Trans. R. Soc. A* **265**, 437–505 (1969).
- Waddington, E. D., Bolzan, J. F. & Alley, R. B. Potential for stratigraphic folding near ice-sheet centers. *J. Glaciol.* **47**, 639–648 (2001).
- NEEM community members Eemian interglacial reconstructed from a Greenland folded ice core. *Nature* **493**, 489–494 (2013).
- Jansen, D. et al. Small-scale disturbances in the stratigraphy of the NEEM ice core: observations and numerical model simulations. *Cryosphere* **10**, 359–370 (2016).
- Westhoff, J. et al. A stratigraphy-based method for reconstructing ice core orientation. *Ann. Glaciol.* **62**, 191–202 (2020).
- Keisling, B. et al. Basal conditions and ice dynamics inferred from radar-derived internal stratigraphy of the northeast Greenland ice stream. *Ann. Glaciol.* **55**, 127–137 (2014).
- Franke, S. et al. Bed topography and subglacial landforms in the onset region of the Northeast Greenland Ice Stream. *Ann. Glaciol.* **61**, 143–153 (2020).
- Bons, P. D. et al. Converging flow and anisotropy cause large-scale folding in Greenland's ice sheet. *Nat. Commun.* <https://doi.org/10.1038/ncomms11427> (2016).
- Laysinger Vieli, G. J.-M. C., Martin, C., Hindmarsh, R. C. A. & Lüthi, M. P. Basal freeze-on generates complex ice-sheet stratigraphy. *Nat. Commun.* <https://doi.org/10.1038/s41467-018-07083-3> (2018).
- Bell, R. E. et al. Widespread persistent thickening of the East Antarctic Ice Sheet by freezing from the base. *Science* **331**, 1592–1595 (2011).
- Creyts, T. T. et al. Freezing of ridges and water networks preserves the Gamburtsev Subglacial Mountains for millions of years. *Geophys. Res. Lett.* **41**, 8114–8122 (2014).
- Wolovick, M. J., Creyts, T. T., Buck, W. R. & Bell, R. E. Traveling slippery patches produce thickness-scale folds in ice sheets. *Geophys. Res. Lett.* **41**, 8895–8901 (2014).
- Wolovick, M. J. & Creyts, T. T. Overturned folds in ice sheets: insights from a kinematic model of traveling sticky patches and comparisons with observations. *J. Geophys. Res. Earth Surf.* **121**, 1065–1083 (2016).
- Panton, C. & Karlsson, N. B. Automated mapping of near bed radio-echo layer disruptions in the Greenland Ice Sheet. *Earth Planet. Sci. Lett.* **432**, 323–331 (2015).

24. Holschuh, N., Christianson, K. & Anandakrishnan, S. Power loss in dipping internal reflectors, imaged using ice-penetrating radar. *Ann. Glaciol.* **55**, 49–56 (2014).
25. Franke, S. et al. Complex basal conditions and their influence on ice flow at the onset of the Northeast Greenland Ice Stream. *J. Geophys. Res. Earth Surf.* **126**, e2020JF005689 (2021).
26. Rasmussen, S. O. et al. A first chronology for the North Greenland Eemian Ice Drilling (NEEM) ice core. *Clim. Past* **9**, 2713–2730 (2013).
27. Joughin, I., Smith, B. E. & Howat, I. M. A complete map of Greenland ice velocity derived from satellite data collected over 20 years. *J. Glaciol.* <https://doi.org/10.1017/jog.2017.73> (2017).
28. Kyrke-Smith, T. M., Katz, R. F. & Fowler, A. C. Stress balances of ice streams in a vertically integrated, higher-order formulation. *J. Glaciol.* **59**, 449–466 (2013).
29. Payne, A. J. & Dongelmanns, P. W. Self-organization in the thermomechanical flow of ice sheets. *J. Geophys. Res.* **102**, 12219–12233 (1997).
30. Hindmarsh, R. C. A. Consistent generation of ice-streams via thermo-viscous instabilities modulated by membrane stresses. *Geophys. Res. Lett.* **36**, L06502 (2009).
31. Schoof C. and Mantelli E. The role of sliding in ice stream formation. *Proc. R. Soc. A* <https://doi.org/10.1098/rspa.2020.0870> (2021).
32. Sayag, R. & Tziperman, E. Interaction and variability of ice streams under a triple-valued sliding law and non-Newtonian rheology. *J. Geophys. Res.* **116**, F01009 (2011).
33. Benn, D., Fowler, A., Hewitt, I. & Sevestre, H. A general theory of glacier surges. *J. Glaciol.* **65**, 701–716 (2019).
34. Karlsson, N. B. & Dahl-Jensen, D. Response of the large-scale subglacial drainage system of Northeast Greenland to surface elevation changes. *Cryosphere* **9**, 1465–1479 (2015).
35. Jacobel, R. W., Scambos, T. A., Raymond, C. F. & Gades, A. M. Changes in the configuration of ice stream flow from the West Antarctic ice sheet. *J. Geophys. Res.* **101**, 5499–5504 (1996).
36. Anandakrishnan, S. & Alley, R. B. Stagnation of Ice Stream C, West Antarctica by water piracy. *Geophys. Res. Lett.* **24**, 265–268 (1997).
37. Conway, H. et al. Switch of flow direction in an Antarctic ice stream. *Nature* **419**, 465–467 (2002).
38. Siegert, M. J. et al. Ice flow direction change in interior West Antarctica. *Science* **305**, 1948–1951 (2004).
39. Larsen, N. K. et al. Instability of the Northeast Greenland Ice Stream over the last 45,000 years. *Nat. Commun.* **9**, 1872 (2018).
40. Lecavalier, B. S. et al. A model of Greenland ice sheet deglaciation constrained by observations of relative sea level and ice extent. *Quatern. Sci. Rev.* **102**, 54–84 (2014).
41. Fahnestock, M., Abdalati, W., Joughin, I., Brozena, J. & Gogineni, P. High geothermal heat flow, basal melt, and the origin of rapid ice flow in central Greenland. *Science* **294**, 2338–2342 (2001).
42. Smith-Johnsen, S., de Fleurian, B., Schlegel, N., Seroussi, H. & Nisancioglu, K. Exceptionally high heat flux needed to sustain the Northeast Greenland Ice Stream. *Cryosphere* **14**, 841–854 (2020).
43. Bons, P. D. et al. Comment on “Exceptionally high heat flux needed to sustain the Northeast Greenland Ice Stream” by Smith-Johnsen et al. (2020). *Cryosphere* **15**, 2251–2254 (2021).
44. Morlighem, M. et al. BedMachine v.3: complete bed topography and ocean bathymetry mapping of Greenland from multibeam echo sounding combined with mass conservation. *Geophys. Res. Lett.* **44**, 11051–11061 (2017).
45. Moon, T., Fisher, M., Harden, L. & Stafford, T. QGreenland v.1.0.0 (National Snow and Ice Data Center, 2021); <https://www.qgreenland.org>

Publisher’s note Springer Nature remains neutral with regard to jurisdictional claims in published maps and institutional affiliations.

Open Access This article is licensed under a Creative Commons Attribution 4.0 International License, which permits use, sharing, adaptation, distribution and reproduction in any medium or format, as long as you give appropriate credit to the original author(s) and the source, provide a link to the Creative Commons license, and indicate if changes were made. The images or other third party material in this article are included in the article’s Creative Commons license, unless indicated otherwise in a credit line to the material. If material is not included in the article’s Creative Commons license and your intended use is not permitted by statutory regulation or exceeds the permitted use, you will need to obtain permission directly from the copyright holder. To view a copy of this license, visit <http://creativecommons.org/licenses/by/4.0/>.

© The Author(s) 2022

Methods

AWI UWB RES data profiles

In April and May 2018, we collected RES data upstream of the northern catchment of 79NG and at the onset of NEGIS with the UWB airborne RES system of AWI (black lines in Fig. 1a–c,g). The system consists of an antenna array with eight channels (co-polarized with the polarization plane oriented in flight direction), and the data were recorded at a frequency range of 180–210 MHz. For a comprehensive description of AWI's UWB RES system and the survey design of the NEGIS survey, see refs. 6,46,47. We used the CReSIS Toolbox⁴⁸ for RES data processing, which includes synthetic aperture radar and array processing^{16,46}. For the geometrical analysis of the IRHs, we depth convert the two-way travel time RES data with a 2D dielectric constant (ϵ) model for air, with a relative permittivity $\epsilon_{\text{air}} = 1$, and ice with $\epsilon_{\text{ice}} = 3.15$.

Construction of 3D horizons

For a 3D analysis of the IRHs, we build on the approach of Bons et al.¹⁷ and use the 3D model-building software MOVE (MOVE Core Application, Version 2019). The radargrams in depth domain were converted to the SEG-Y format with the ObsPy Python toolbox⁴⁹ and imported into MOVE. Internal layers, which could be clearly identified in all RES sections, were traced manually. The traced layers were split into segments that show similar geometries (for example, anticlines and synclines) as segments of the same IRH in adjacent radargrams. For this purpose, the optimal orientation of the radar profiles is perpendicular (90°) to the fold axes, which approximately applies to the reconstruction of the 3D surfaces at Petermann¹⁷ as well as to the reconstruction of the Set 1 folds. Supplementary Fig. 30a shows how the line segments are interpolated between a pair of radargrams.

We express the degree of deformation of the 3D horizons with depth by comparing the area of the horizons for a specific region. The area with zero deformation (analogous to the horizons at initial deposition) is represented by a polygon with the extent of the referenced region (Supplementary Fig. 30c). The area of a distorted horizon is larger than the area of the polygon. The degree of deformation is then expressed by the ratio in percentage terms. The method generally underestimates the degree of deformation unless the layers between the folded horizons do not thicken.

Fold axial surfaces

We construct the axial surfaces of one anticline and two synclines that make up the cylindrical folds of Set 1 (Figs. 1c and 2). The method is analogous to the construction of the 3D horizons (Supplementary Fig. 30b). We trace the points of maximum curvature in the radargrams for two synclines and the anticline of the cylindrical fold to create a line segment and interpolate between the lines of each radargram.

Ice-flow reconstruction from axial traces

Due to the curvature of the fold axial traces, we define a minimum and a maximum distance for a measure of the displacement of the ice column (dS_{min} and dS_{max}) for five profiles of synclines 1 and 2, respectively (Fig. 2a). At each position, we use the absolute ice-flow velocity (v_s) to calculate the velocity component parallel to the direction of shearing with the offset angle α : $v_y = v_s \cos(\alpha)$ (Supplementary Fig. 31 and Supplementary Table 1). We assume that the ice-flow velocity has not changed over time and varies only slightly in space. Then we calculate the time needed for the displacement of the upper ice column t_s , assuming that the deepest end of the axial trace is immobile: $t_s = \frac{dS}{v_y}$. The vector components of the velocity field are shown in Supplementary Fig. 31a.

Data availability

The CReSIS RES data used in this study are available under CReSIS data products (<https://data.cresis.ku.edu/data/rds/>). AWI UWB RES data of the EGRIP-NOR-2018 campaign at the NEGIS⁴⁶ onset are available at

PANGAEA (<https://doi.org/10.1594/PANGAEA.928569>). The AWI UWB RES data of Set 1 are available at Pangaea via <https://doi.org/10.1594/PANGAEA.949391> and the AWI EMR RES data in Set 2 are available via <https://doi.org/10.1594/PANGAEA.949619>. A list of all RES profiles is provided in Supplementary Tables 2–4. AWI UWB ice-thickness data from Set 1⁵⁰ are available at PANGAEA (<https://doi.org/10.1594/PANGAEA.913193>). All AWI RES derived ice-thickness data used in this study are already included in the BMv3 dataset⁴⁴.

References

46. Franke, S. et al. Airborne ultra-wideband radar sounding over the shear margins and along flow lines at the onset region of the Northeast Greenland Ice Stream. *Earth Syst. Sci. Data* **14**, 763–779 (2022).
47. Hale, R. et al. Multi-channel ultra-wideband radar sounder and imager. In *Proc. IEEE International Geoscience and Remote Sensing Symposium (IGARSS)* <https://doi.org/10.1109/IGARSS.2016.7729545> (2016).
48. CReSIS Toolbox (CReSIS, 2020); <https://github.com/CReSIS/>
49. Beyreuther, M. et al. ObsPy: a Python toolbox for seismology. *Seismol. Res. Lett.* **81**, 530–533 (2010).
50. Jansen, D., Franke, S., Binder, T., Helm, V. & Paden, J. D. *Ice Thickness from the Northern Catchment Region of Greenland's 79 North Glacier, Recorded with the Airborne AWI UWB Radar System* (Alfred Wegener Institute, Helmholtz Centre for Polar and Marine Research, PANGAEA, 2020); <https://doi.org/10.1594/PANGAEA.913193>
51. Förste, C. et al. The GeoForschungsZentrum Potsdam/Groupe de Recherche de Géodésie Spatiale satellite-only and combined gravity field models: EIGEN-GLO4S1 and EIGEN-GLO4C. *J. Geod.* **82**, 331–346 (2008).
52. MacGregor, J. A. et al. A synthesis of the basal thermal state of the Greenland Ice Sheet. *J. Geophys. Res. Earth Surf.* **121**, 1328–1350 (2016).
53. Jordan, T. M. et al. A constraint upon the basal water distribution and thermal state of the Greenland Ice Sheet from radar bed echoes. *Cryosphere* **12**, 2831–2854 (2018).

Acknowledgements

We thank the crew of the research aircraft Polar 6 and system engineers M. Gehrman and L. Kandora. We acknowledge using RES data from CReSIS generated with support from the University of Kansas, NASA Operation IceBridge grant NNX16AH54G, NSF grants ACI-1443054, OPP-1739003 and IIS-1838230, Lilly Endowment Incorporated and Indiana METACyT Initiative. We thank the EGRIP project for logistical support during the EGRIP-NOR-2018 RES campaign. EGRIP is directed and organized by the Centre for Ice and Climate at the Niels Bohr Institute, University of Copenhagen. It is supported by funding agencies and institutions in Denmark (A. P. Møller Foundation, University of Copenhagen), the United States (US National Science Foundation, Office of Polar Programs), Germany (Alfred Wegener Institute, Helmholtz Centre for Polar and Marine Research), Japan (National Institute of Polar Research and Arctic Challenge for Sustainability), Norway (University of Bergen and Trond Mohn Foundation), Switzerland (Swiss National Science Foundation), France (French Polar Institute Paul-Emile Victor, Institute for Geosciences and Environmental Research), Canada (University of Manitoba) and China (Chinese Academy of Sciences and Beijing Normal University). We acknowledge the National Snow and Ice Data Center QGreenland package. Moreover, we thank Emerson E&P Software, Emerson Automation Solutions, for providing licences in the scope of the Emerson Academic Program. S.F. was funded by the AWI Strategy fund, and D.J. was funded by the AWI Strategy Fund and the Helmholtz Young Investigator Group HGF YIG VH-NG-802. J.W. was funded by the Villum Investigator Project IceFlow (NR. 16572).

Author contributions

S.F., P.D.B. and D.J. wrote the manuscript. S.F. processed the RES data with contributions of J.D.P., constructed the 3D horizons and performed all calculations and analyses. D.J. designed the study and developed the scientific idea with contributions of P.D.B., I.W. and S.F. D.J. was principal investigator on the airborne RES survey, and T.B. and V.H. collected the data. D.S. provided additional ice-thickness data, and V.H. assisted with GPS post processing. J.W. developed the idea for the visualization for the fold deformation stages and developed the folding hypothesis together with P.D.B., D.J., I.W. and S.F. O.E., D.S., V.H., G.E., K.S. and I.W. provided detailed feedback on the analyses. All authors discussed and reviewed the manuscript.

Funding

Open access funding provided by Alfred-Wegener-Institut

Competing interests

The authors declare no competing interests.

Additional information

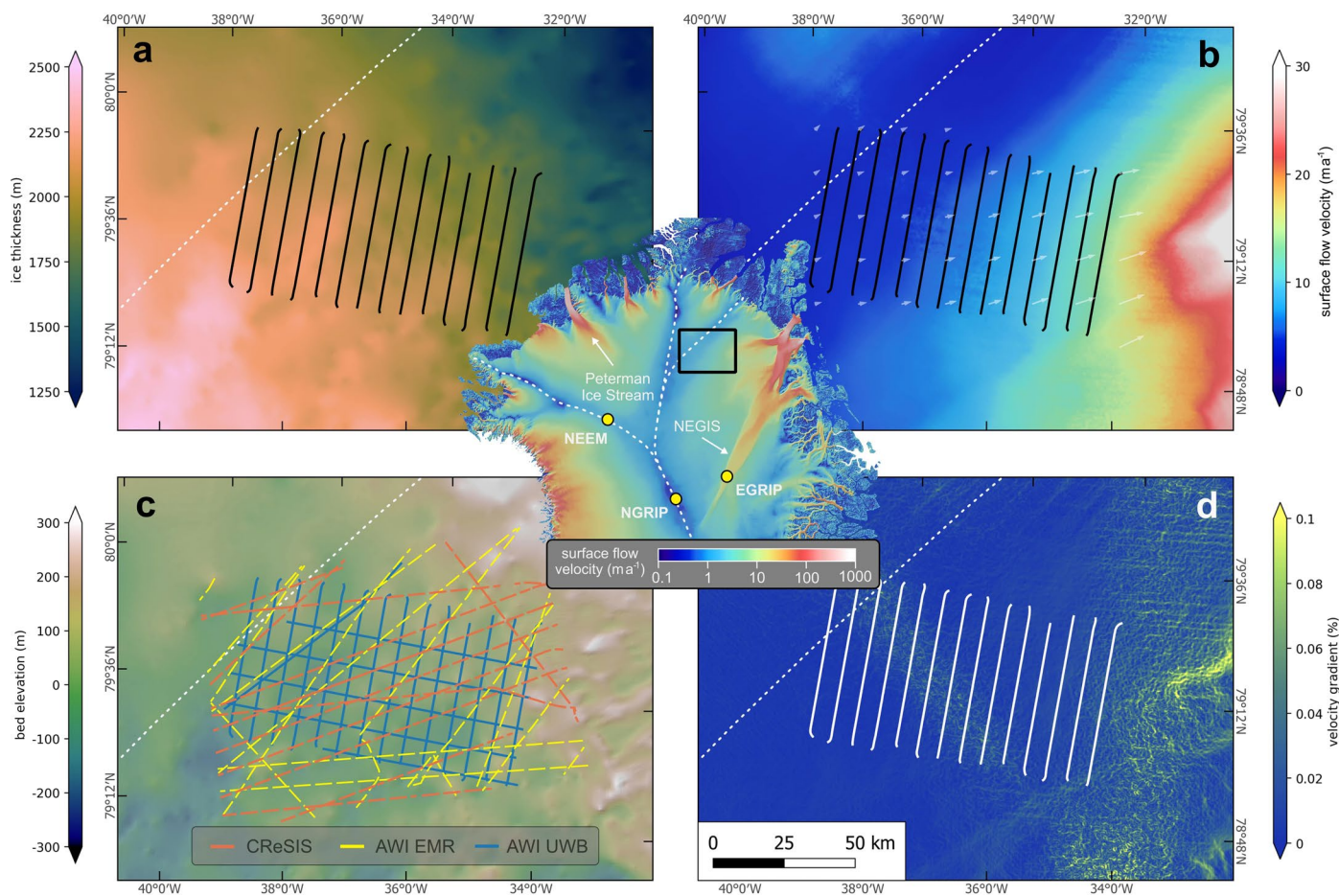
Extended data is available for this paper at <https://doi.org/10.1038/s41561-022-01082-2>.

Supplementary information The online version contains supplementary material available at <https://doi.org/10.1038/s41561-022-01082-2>.

Correspondence and requests for materials should be addressed to Steven Franke.

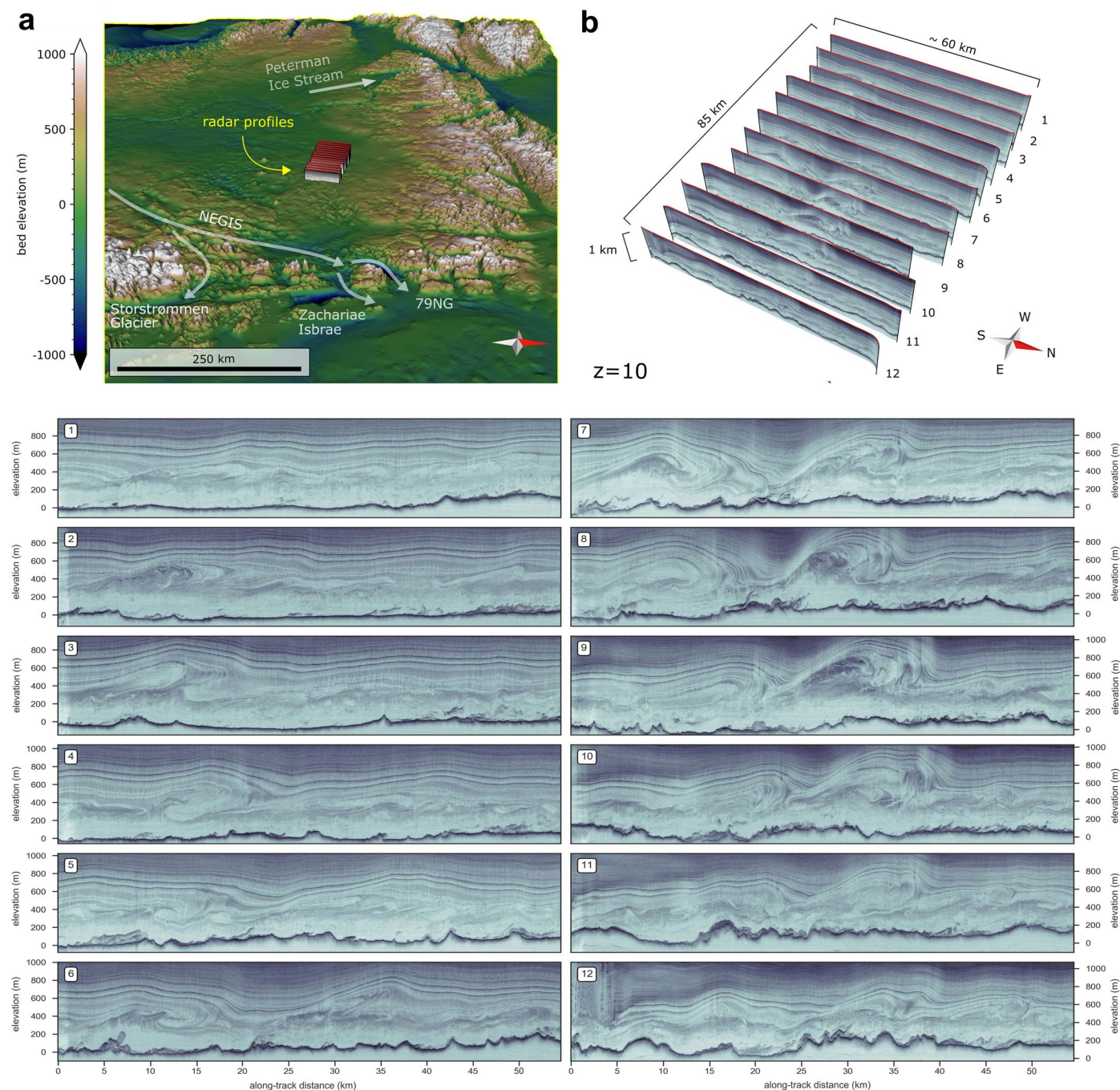
Peer review information *Nature Geoscience* thanks Richard Hindmarsh, Neil Ross and the other, anonymous, reviewer(s) for their contribution to the peer review of this work. Primary Handling Editor: James Super, in collaboration with the *Nature Geoscience* team.

Reprints and permissions information is available at www.nature.com/reprints.



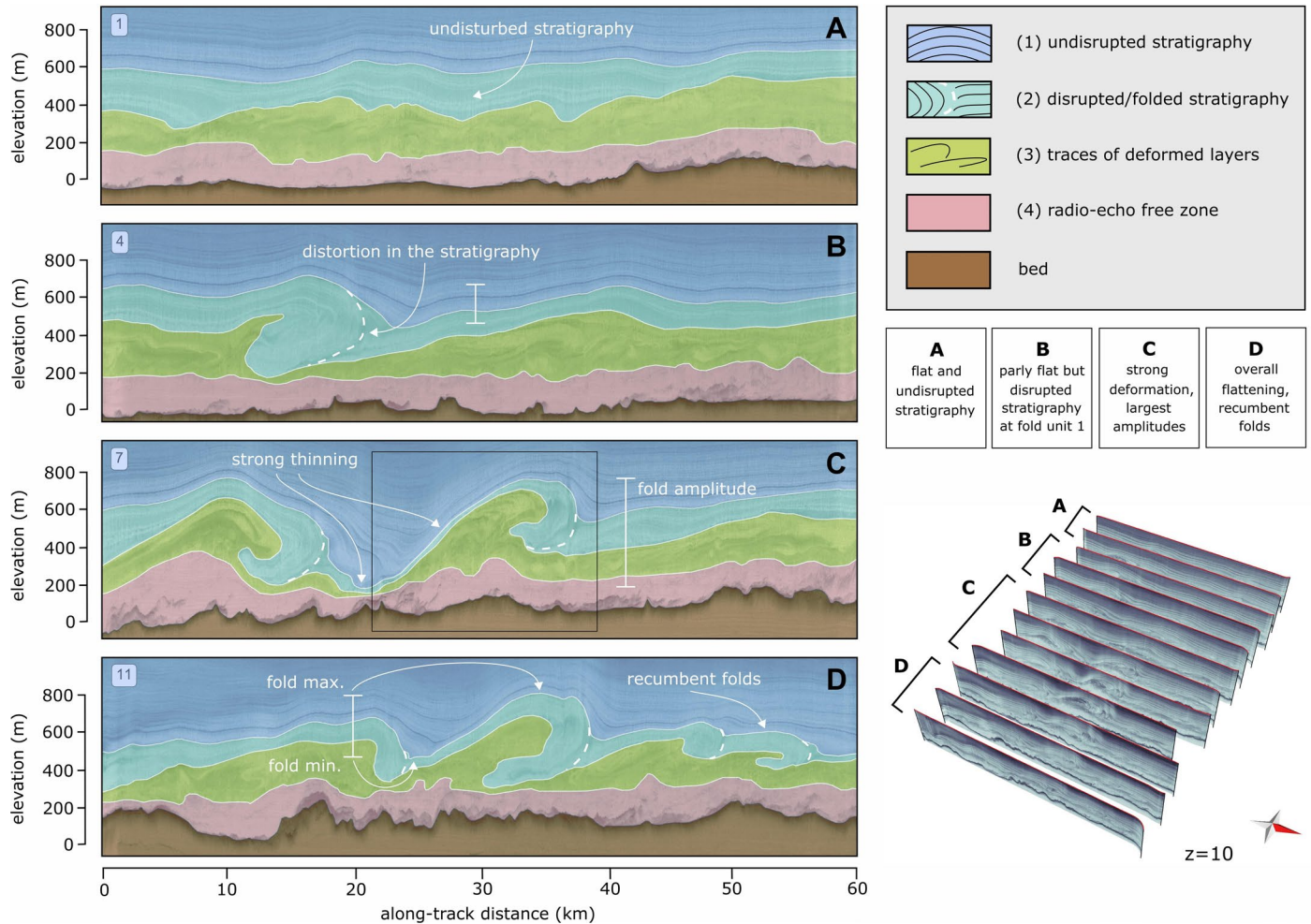
Extended Data Fig. 1 | Location of Set 1 radar profiles in Northern Greenland. The central map shows the location of the survey area (black outline) as well as the ice surface velocity²⁷, the location of the deep drill sites (yellow dots), the location of the North East Greenland Ice Stream (NEGIS) and the Petermann Ice Stream. The lines in **a**, **b** and **d** represent the survey lines, which were used for the 3D IRH reconstruction. The white dashed lines represent the main ice divides. Panels **a** and **c** represent the ice thickness and bed elevation from the BedMachine v3 (BMv3)⁴⁴ data set, respectively. Panel **b** shows the ice surface velocity and flow

direction²⁷ and **d** the velocity gradient. Panel **c** shows profiles of radar-derived ice thickness data, which were used for the generation of an improved bed elevation model (Supplementary Fig. 14). Dashed red and yellow lines in **c** represent ice thickness data that is already included in BMv3. The solid blue lines are new ice thickness data from this survey. The bed elevation is referenced to the mean sea level using the geoid EIGEN-6C4⁵¹. This map and all the following maps in Extended Data Figures are shown in EPSG:3413 (WGS 84/NSIDC Sea Ice Polar Stereographic North).



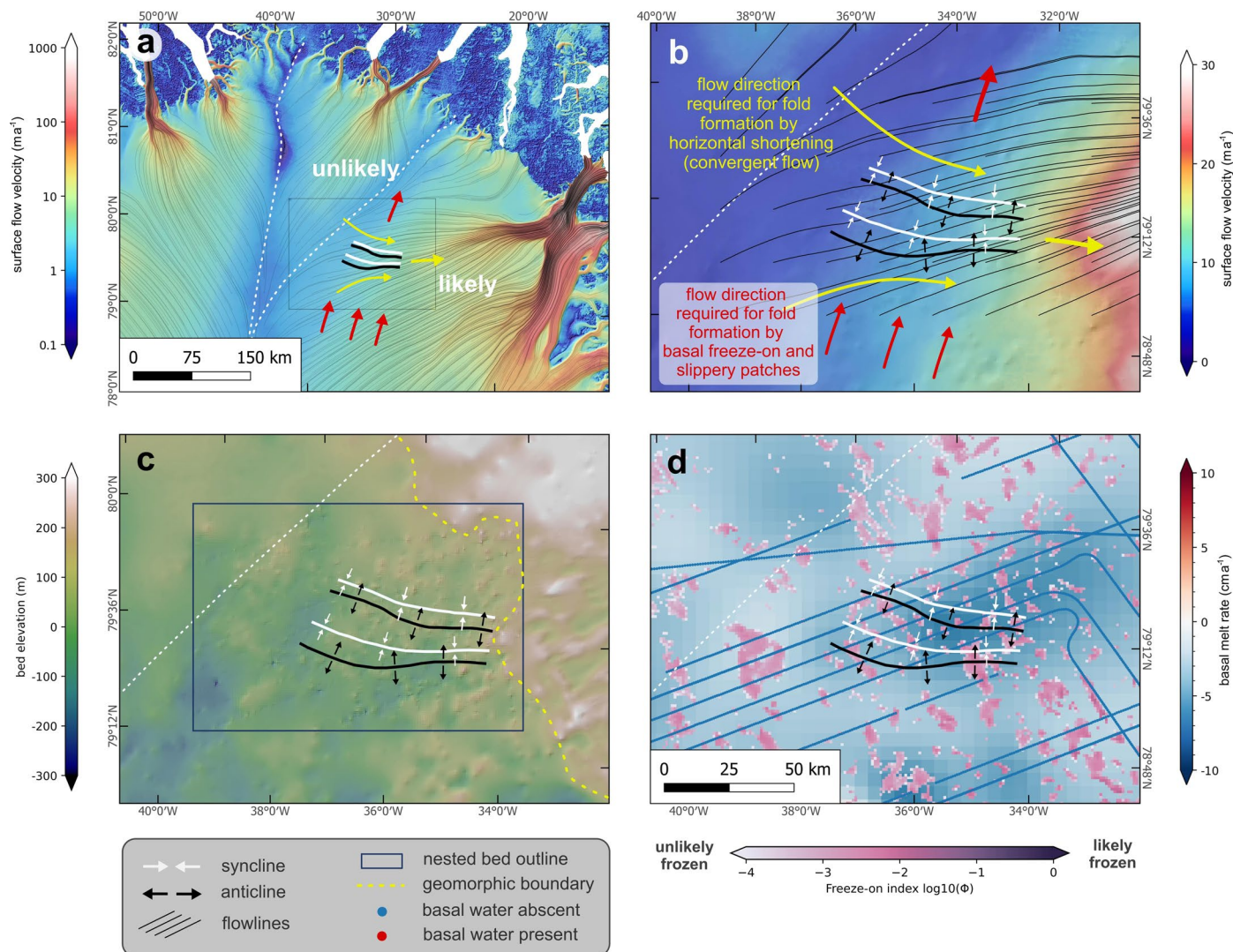
Extended Data Fig. 2 | Radar profiles showing the deep radio-stratigraphy of Set 1. Panel a shows a 3D canvas with the location and orientation of the radar profiles in relation to the bed topography of Greenland. The bed elevation is

taken from the BedMachine v3 data set⁴⁴. Panel b and subfigures 1–12 show lower stratigraphy of the single radar sections. The full radargrams are shown in the Supplementary Fig. 1–12. The vertical exaggeration factor (z) of all images is 10.



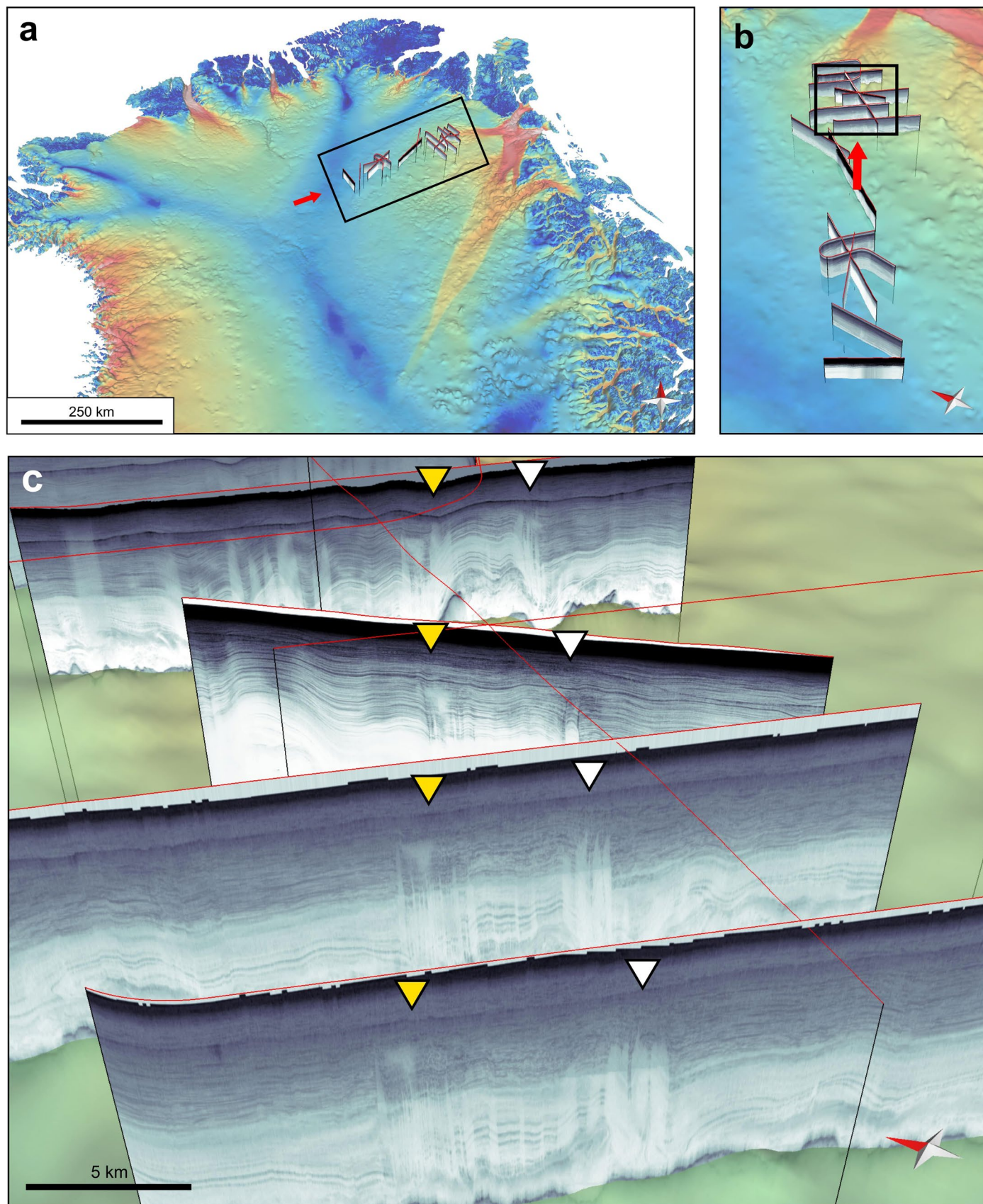
Extended Data Fig. 3 | Schematic view of the deep radio-stratigraphy of Set 1. Panels A–D in the radargrams on the left represent examples of the four different schematic deformation stages. The respective numbers of the radar profiles are indicated in the upper left corner and correspond to the numbers in Extended Data Fig. 2. The corresponding overview of all individual radargrams, which show these deformation stages are shown in the lower right. The radio-stratigraphy in the radargrams of Set 1 comprises four-layered units (units 1–4 in A–D). The uppermost unit (1) consists of ice with undisturbed internal layer stratigraphy. Radar reflections in the underlying unit (2) are visible in all radargrams but are disrupted where folds overturn (B and C). Unit (3) below this

is located above the basal unit (4) and shows non-continuous reflectors. Unit (4) is devoid of reflections. Radargrams close to the ice divide show horizontally layered strata and the least deformation of all profiles (A). The central radar profiles show two large overturned folds (anticline-syncline pairs) whose amplitudes increase downwards through the ice column. Amplitude height also increases downwards until they reach maxima of 500–600 m (D). The folds are upright in the upper part of the ice column and become increasingly recumbent downwards, an indication of bedrock-parallel shearing. The number of folds in the radar profiles increases downstream whereas their wavelength decreases.



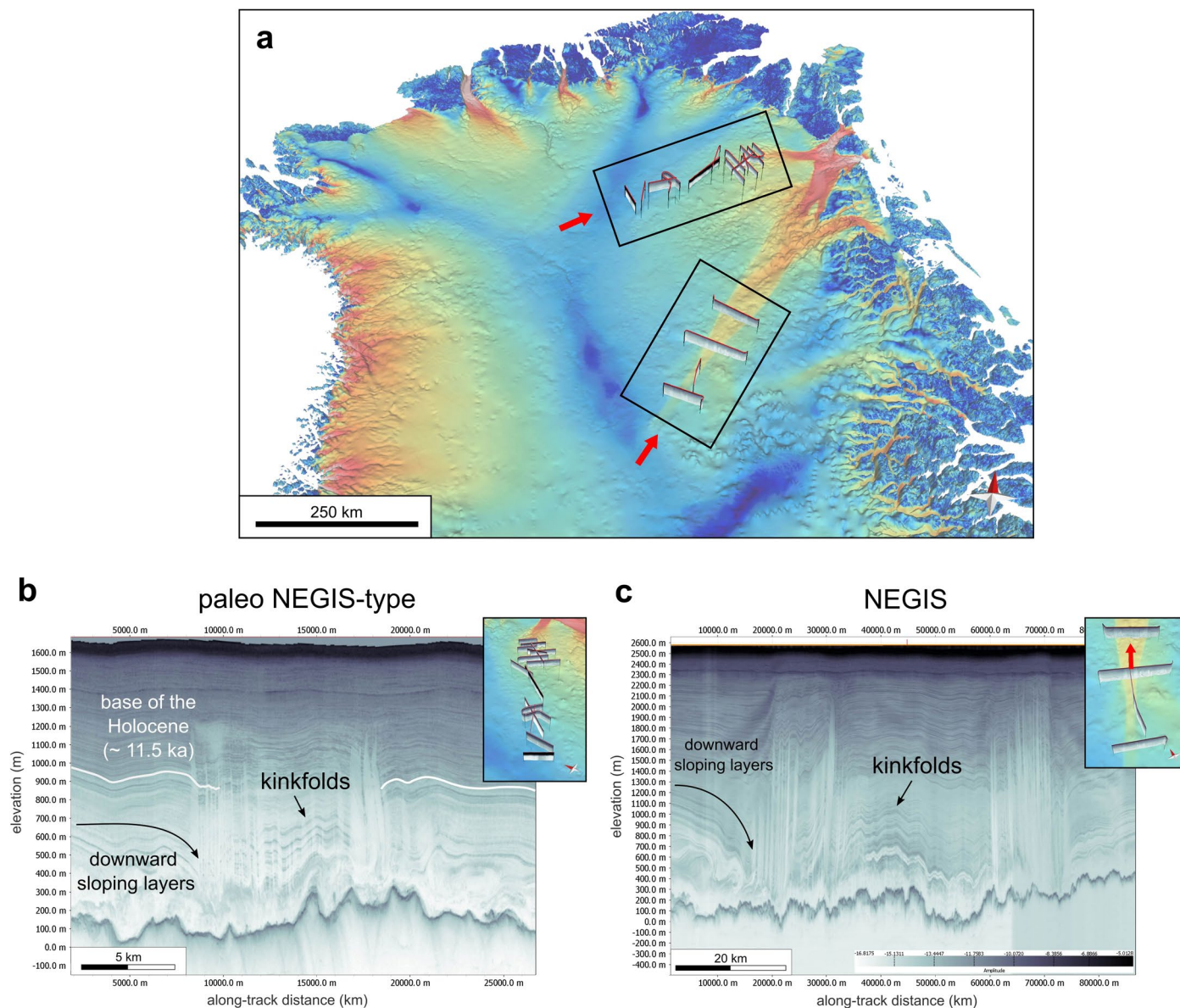
Extended Data Fig. 4 | Set 1 folds with their ice-dynamic and basal properties context. Panel **a** shows the ice surface velocity²⁷ of northern Greenland on the logarithmic scale (\log_{10}) as well as flow lines and the position and orientation of the folds (here displayed with the syncline and anticline fold axes). **b** shows a magnified view of the surface flow velocity on a linear scale as well as flow lines superimposed on the bed topography hillshade⁴⁴. The red and yellow arrows in **a** and **b** indicate the respective required ice flow direction for fold formation via slippy patches and basal freeze-on (red arrows) or alternatively by convergent

flow (yellow arrows). Panel **c** shows the relation between fold location and bed elevation. The boundary between the western bedrock morphology (low bed elevation) and the eastern morphology (higher bed elevation and subglacial landforms) is indicated with yellow dots. Panel **d** indicates basal melt rate of MacGregor et al.⁵² in the background color code, and constraints of basal water by Jordan et al.⁵³, where blue dots represent the absence of basal water and red dots the presence of basal water (which is not the case in this region) and the freeze-on index by Leisinger Vieli et al.¹⁸.



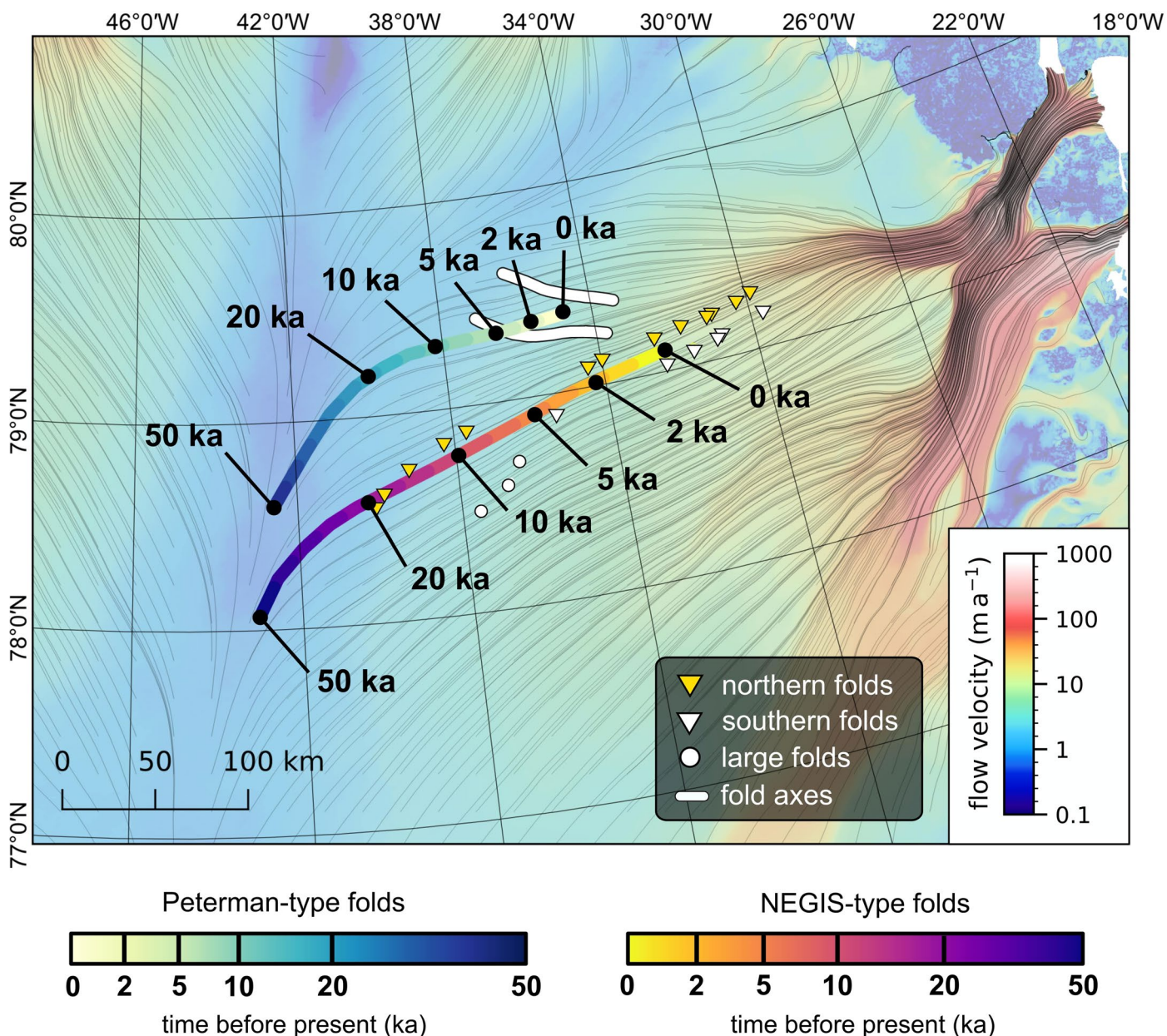
Extended Data Fig. 5 | Repetitive shear margin fold pattern in Set 2 radargrams. Panel a shows a 3D canvas with the bed topography⁴⁴ overlain with the ice surface flow velocity field²⁷ (same color code as in Fig. 1b in the main document) and the radargrams of Set 2. The red arrow in this and the following images illustrates the point of view of the neighboring image in b and other

images. c shows a zoomed in view on the bed topography overlain with the ice surface flow velocity field (same as in a) and the radargrams. The radargrams in this image are located further downstream and the shear margin signature is highlighted with yellow and white triangles.



Extended Data Fig. 6 | Shear margin radar signature comparison. Panel **a** shows a 3D canvas with the bed topography⁴⁴ overlain with the ice surface flow velocity²⁷, the radargrams of Set 2 and radargrams at the onset region of the NEGIS. **b** and **c** show a comparison of the fold pattern in the upstream part of Set 2 (paleo NEGIS-type; **b**) and at the onset of the NEGIS (**c**). In the radargrams we

highlight the similarities in the radar stratigraphy, such as kinkfolds between the tightly folded sequences and downward sloping internal layers at the margins of the tight folds. In **b** we furthermore mark the isochrone representing the transition from the Holocene to the Glacial (white line).



Extended Data Fig. 7 | Backtracking of fold patterns. Two examples of the possible propagation pathways of internal deformation features over time along a flow line for the paleo Petermann-type and NEGIS-type ice flow regime. The ice surface flow velocity and the flow lines in the background are obtained from²⁷. After shutdown of active folding due to the Petermann-type and NEGIS-type ice stream regime, the internal deformation features will be transported

downstream. Here we present an estimate on the duration and propagation of one respective location for both paleo ice-stream features (location of the feature shown at the 0 ka marker) along a flow line of the present ice surface flow field from²⁷. The propagation distance depends on how long the two paleo ice-flow regimes have been inactive and with the assumption that the subsequent flow regime is the present one.